An All-Silicon Passive Optical Diode

Li Fan *et al.*

Science **335**, 447 (2012);
DOI: 10.1126/science.1214383

Science (print ISSN 0036-8075; online ISSN 1095-9203) is published weekly, except the last week in December, by the American Association for the Advancement of Science, 1200 New York Avenue NW, Washington, DC 20005.

vents contributes appreciably to improved energy efficiency in recovery of the solvents. A range of industries—including polymer synthesis (*23*), production of biofuels (*24*), environmental remediation (*25*), and oil extraction in the food industry (*19*)—have a strong demand for solvent-resistant nanofiltration membranes with superior permeability characteristics. For these purposes, nanoporous free-standing sheets of carbon nanotubes (*26*, *27*) and other inorganic membranes (*28*) have been studied globally. However, it has been a challenge to produce such membranes in an industrially applicable process. DLC membranes have been found to be extremely dense and suitable for use in gas barrier applications (*29*, *30*). In this Report, we demonstrate that DLC membranes can be prepared with extremely high solvent permeability while maintaining considerable mechanical strength.

References and Notes

1. K. R. Buck, V. K. Davar, *Br. Polym. J.* **2**, 238 (1970).
2. J. R. Hollahan, T. Wydeven, *Science* **179**, 500 (1973).
3. H. Yasuda, C. E. Lamaze, *J. Appl. Polym. Sci.* **17**, 201 (1973).
4. A. A. Bondi, *Physical Properties of Molecular Crystals, Liquids, and Glasses* (Wiley, New York, 1968).
5. D. W. Van Krevelen, *Properties of Polymers* (Elsevier, Amsterdam, 1990).
6. Y. H. See Toh, F. W. Lim, A. G. Livingston, *J. Membr. Sci.* **301**, 3 (2007).
7. M. Kiyono, P. J. Williams, W. J. Koros, *J. Membr. Sci.* **359**, 2 (2010).
8. A. F. Ismail, D. Rana, T. Matsuura, H. C. Foley, *Carbon-Based Membranes for Separation Processes* (Springer, New York, 2011).
9. S. Aisenberg, R. Chabot, *J. Appl. Phys.* **42**, 2953 (1971).
10. J. Robertson, *Mater. Sci. Eng. Rep.* **37**, 129 (2002).
11. X. D. Pan, E. A. Maydell, R. H. Milne, D. J. Fabian, *Vacuum* **41**, 1360 (1990).
12. I. Ichinose, K. Kurashima, T. Kunitake, *J. Am. Chem. Soc.* **126**, 7162 (2004).
13. M. Werner, S. Hein, E. Obermeier, *Diamond Relat. Mater.* **2**, 939 (1993).
14. We used the term of DLC to emphasize the mechanical stability of the membranes. However, the fraction of sp^2 carbon is relatively high and is close to that in disordered carbon (see SOM).
15. P. Koidl, Ch. Wild, B. Dischler, J. Wagner, M. Ramsteiner, *Mater. Sci. Forum* **52-53**, 41 (1990).
16. P. J. R. Honeybone, R. J. Newport, J. K. Walters, W. S. Howells, J. Tomkinson, *Phys. Rev. B* **50**, 839 (1994).
17. K. Li, *Ceramic Membranes for Separation and Reaction* (Wiley, West Sussex, UK, 2007).
18. Q. Zhang, S. Ghosh, S. Samitsu, X. Peng, I. Ichinose, *J. Mater. Chem.* **21**, 1684 (2011).
19. P. Silva, L. G. Peeva, A. G. Livingston, in *Advanced Membrane Technology and Applications*, N. N. Li, A. G. Fane, W. S. W. Ho, T. Matsuura, Eds. (Wiley, Hoboken, NJ, 2008), pp. 451–467.
20. J. L. Anderson, J. A. Quinn, *Biophys. J.* **14**, 130 (1974).
21. G. F. Froment, K. B. Bischoff, *Chemical Reactor Analysis and Design* (Wiley, New York, 1979).
22. P. Vandezande, L. E. M. Gevers, I. F. J. Vankelecom, *Chem. Soc. Rev.* **37**, 365 (2008).
23. S. So, L. G. Peeva, E. W. Tate, R. J. Leatherbarrow, A. G. Livingston, *Org. Process Res. Dev.* **14**, 1313 (2010).
24. R. Othman, A. W. Mohammad, M. Ismail, J. Salimon, *J. Membr. Sci.* **348**, 287 (2010).
25. I. C. Escobar, S. Hong, A. Randall, *J. Membr. Sci.* **175**, 1 (2000).
26. J. K. Holt *et al.*, *Science* **312**, 1034 (2006).
27. F. Fornasiero *et al.*, *Proc. Natl. Acad. Sci. U.S.A.* **105**, 17250 (2008).
28. C. C. Striemer, T. R. Gaborski, J. L. McGrath, P. M. Fauchet, *Nature* **445**, 749 (2007).
29. A. Shirakura *et al.*, *Thin Solid Films* **494**, 84 (2006).
30. G. A. Abbas, S. S. Roy, P. Papakonstantinou, J. A. McLaughlin, *Carbon* **43**, 303 (2005).

Acknowledgments: We gratefully acknowledge financial support from JST, CREST, and a grant-in-aid for scientific research from the Ministry of Education, Culture, Sports, Science and Technology, Japan (no. 23350105). A part of this Report was used for a Japanese patent [application no. (2010) 180194].

Supporting Online Material

www.sciencemag.org/cgi/content/full/335/6067/444/DC1
Materials and Methods
Figs. S1 to S15
Tables S1 to S3
References (*31*–*55*)

2 August 2011; accepted 7 November 2011
10.1126/science.1212101

An All-Silicon Passive Optical Diode

Li Fan,[1,2]* Jian Wang,[1,2]* Leo T. Varghese,[1,2]* Hao Shen,[1,2] Ben Niu,[1,2] Yi Xuan,[1,2] Andrew M. Weiner,[1,2] Minghao Qi[1,2,3]†

A passive optical diode effect would be useful for on-chip optical information processing but has been difficult to achieve. Using a method based on optical nonlinearity, we demonstrate a forward-backward transmission ratio of up to 28 decibels within telecommunication wavelengths. Our device, which uses two silicon rings 5 micrometers in radius, is passive yet maintains optical nonreciprocity for a broad range of input power levels, and it performs equally well even if the backward input power is higher than the forward input. The silicon optical diode is ultracompact and is compatible with current complementary metal-oxide semiconductor processing.

Nonreciprocal transmission is fundamental to information processing. Electrical nonreciprocity, or the diode effect, had been realized in integrated form with a semiconductor p-n junction. Optical nonreciprocity (ONR) is inherently difficult because of the time-reversal symmetry of light-matter interaction (*1*). Previously reported observations of ONR were based on the magneto-optic effect (*2*–*4*), optical nonlinearity (*5*–*8*), electro-absorption modulation (*9*), cholesteric liquid crystals (*10*), optomechanical cavities (*11*), indirect interband photonic transitions (*12*), and the opto-acoustic effect (*13*). However, complementary metal-oxide semiconductor (CMOS)–compatible passive optical diodes with a footprint and functionality analogous to those of p-n junctions have not been realized at the near-infrared wavelengths that are preferred for silicon (Si) photonics.

Our optical diode (Fig. 1A) is based on strong optical nonlinearity in high–quality factor (Q) Si microrings (*14*–*17*). It consists of a high-Q all-pass notch filter (NF) operating near the critical coupling regime (*17*) (Fig. 1B) and an add-drop filter (ADF) (*14*, *16*, *18*) with asymmetric power coupling to the bus waveguides (Fig. 1C). The resonant wavelength of the NF is thermally tuned to match that of the ADF through the thermo-optic effect of silicon (*19*).

A microring accumulates optical energy at its resonant wavelength. The schematics in Fig. 1, E and F, show that light couples into the microring in the ADF through two different gaps, G_2 and G_3. If we define forward and backward input power as $P_{c,f}$ and $P_{in,b}$, respectively, the optical energy stored in the microring near its resonant wavelength, λ_{ADF}, can be expressed as

$$U_{\text{forward}}(\lambda) = \frac{P_{c,f}}{Q_{G_2}} Q_{ADF}^2 K(\lambda) \qquad (1)$$

and

$$U_{\text{backward}}(\lambda) = \frac{P_{in,b}}{Q_{G_3}} Q_{ADF}^2 K(\lambda) \qquad (2)$$

where Q_{ADF} is the ring's loaded quality factor, Q_{G_2} and Q_{G_3} are power coupling quality factors that are exponentially proportional to the gap sizes, and $K(\lambda)$ represents all other terms that are independent of propagation direction for a linear system (*14*).

The energy enhancement factor in the ring depends on the propagation direction because of our asymmetric design ($Q_{G_2} \approx 300{,}000$, $Q_{G_3} \approx 192{,}000$, and $Q_{ADF} \approx 43{,}800$, all through curve-fitting), and $(U_{\text{forward}}/U_{\text{backward}}) = (Q_{G_3}/Q_{G_2}) = 0.64$ for $P_{c,f} = P_{in,b}$. With high input power at $\lambda_0 = \lambda_{ADF}$, the power density inside the ring will be amplified substantially because of its high Q factors and small radius; this induces optical nonlinearity in silicon (*20*–*23*) and a red shift in the ring's resonance ($\lambda'_{ADF} > \lambda_0$, Fig. 1F). Because less energy is stored in the ring during forward

[1]Birck Nanotechnology Center, Purdue University, West Lafayette, IN 47907, USA. [2]School of Electrical and Computer Engineering, Purdue University, West Lafayette, IN 47907, USA. [3]Shanghai Institute of Microsystem and Information Technology, Chinese Academy of Sciences, Shanghai 20050, China.

*These authors contributed equally to this work.
†To whom correspondence should be addressed. E-mail: mqi@purdue.edu

propagation, the amount of resonance shift in the forward direction is smaller than that in the backward direction. If we define wavelength detuning as $\delta_{ADF}(\lambda_0) = 2Q_{ADF}[(\lambda_0 - \lambda'_{ADF})/\lambda'_{ADF}]$, we have $|\delta_{ADF,forward}(\lambda_0)| < |\delta_{ADF,backward}(\lambda_0)|$. This leads to a case in which forward transmission, $T_{ADF,forward}(\lambda_0)$, exceeds backward transmission, $T_{ADF,backward}(\lambda_0)$, because

$$T_{ADF,\,forward}(\lambda_0) = \frac{1}{\delta^2_{ADF,\,forward}(\lambda_0) + 1} F \quad (3)$$

and

$$T_{ADF,\,backward}(\lambda_0) = \frac{1}{\delta^2_{ADF,\,backward}(\lambda_0) + 1} F \quad (4)$$

where $F = 4Q^2_{ADF}/Q_{G_2}Q_{G_3}$ is a constant that is independent of propagation direction. Therefore, an ADF with asymmetric power coupling can function as an ONR device for strong optical inputs, and we call it the ONR initiator.

For the NF, the power transmission near its resonance (λ_{NF}) is

$$T_{NF}(\lambda_0) = \frac{\delta^2_{NF}(\lambda_0) + [1 - (2Q_{NF}/Q_{G_1})]^2}{\delta^2_{NF}(\lambda_0) + 1} \quad (5)$$

where Q_{NF} is the loaded quality factor of the NF ring and $\delta_{NF}(\lambda_0) = 2Q_{NF}[(\lambda_0 - \lambda_{NF})/\lambda_{NF}]$ is wavelength detuning. Our design leads to $Q_{G_1} \approx$ 55,000 (*24*), and the fabricated NF ring (*25*) has $Q_{NF} \approx$ 27,000, so $[1 - (2Q_{NF}/Q_{G_1})] \approx 0$. A weak input will pass the NF with a strong attenuation of ~20 dB at $\lambda_0 = \lambda_{NF}$ because $\delta_{NF}(\lambda_0) = 0$. A strong input will red-shift the NF ring ($\lambda'_{NF} > \lambda_0$), resulting in a nontrivial $\delta'_{NF}(\lambda_0)$, and will pass the NF with a much smaller attenuation at λ_0 (Fig. 1D). We call the NF an ONR amplifier because it will significantly attenuate the weakened signal that has passed the ONR initiator in the backward direction.

When we cascade the ONR amplifier to an ONR initiator with similar onset power for nonlinearity (Fig. 1A), strong ONR can be achieved for a broad range of forward and backward input power levels. Without nonlinear effects (i.e., at a very low input power of ~85 nW at the device, with 1 μW measured at the input laser), our optical diode has a transmission that is independent of propagation direction (Fig. 1H).

With the input power increased to ~85 μW, a nonreciprocal transmission ratio (NTR) of ~20 dB was observed at $\lambda_0 = 1630$ nm (Fig. 1I). For forward propagation, input from port I enters the NF first and has sufficiently high power to red-shift the NF resonance, thus allowing it to pass with low attenuation at wavelength λ_0 (solid curve in Fig. 1D). When this input reaches the ADF, the optical energy accumulated in the ADF ring is not high enough to appreciably red-shift the resonance—that is, $\delta_{ADF,forward}(\lambda_0) \rightarrow 0$ in Eq. 3—because of the large gap of G_2 as well as the power reduction after passing the NF. Thus, light can transmit to the drop port through the resonance and achieve reasonably high transmis-

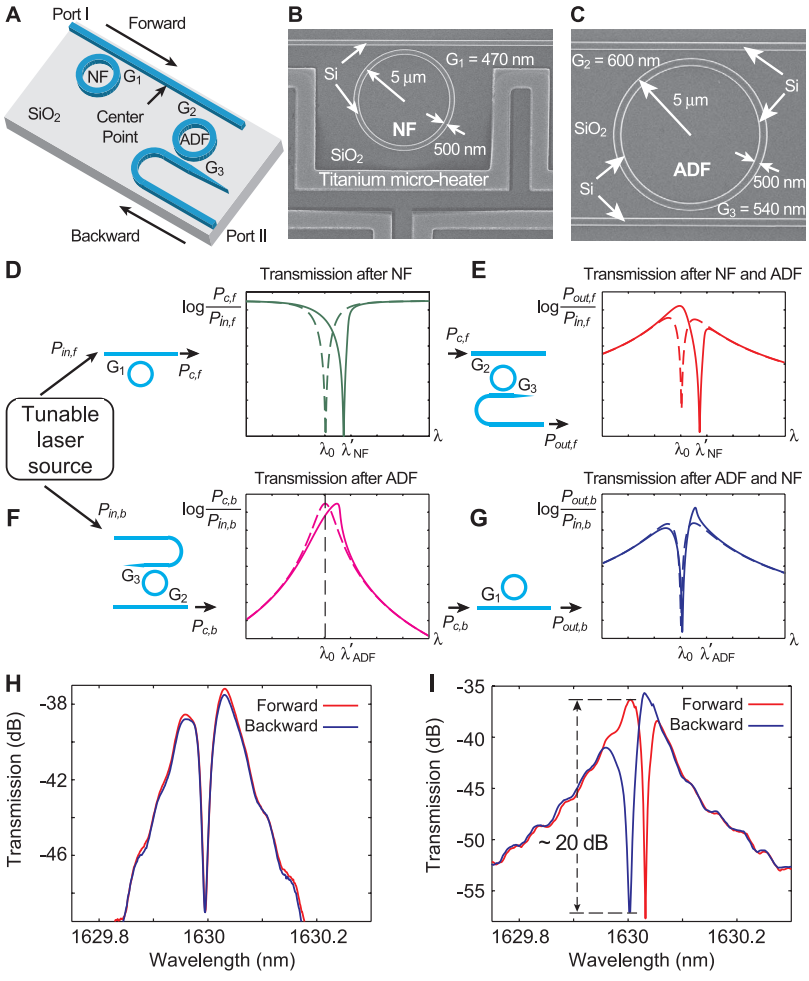

Fig. 1. (**A**) The optical diode consists of two resonance-matched filters: one notch filter (NF) and one add-drop filter (ADF). Input at port I and output at port II is defined as forward propagation; input at port II and output at port I is defined as backward propagation. (**B** and **C**) Fabricated NF and ADF showing the design parameters. A titanium heater allows tuning of the NF resonance to match that of the ADF. (**D** to **G**) Mechanism of passive ONR due to nonlinearity. The optical power at port I, center point, and port II are defined as $P_{in,f}$, $P_{c,f}$, and $P_{out,f}$ for forward propagation and as $P_{out,b}$, $P_{c,b}$, and $P_{in,b}$ for backward propagation. Dashed curves are the simulated transmission spectra in the linear regime (incident power ~85 nW); the solid curves are the simulated transmission spectra at a power level of ~85 μW, which is high enough to induce optical nonlinearity. (**H**) Forward and backward transmission spectra of the diode at ~85 nW incident power, showing reciprocity and good agreement with dashed curves in (E) and (G). (**I**) Forward and backward transmission spectra at input power level of ~85 μW, showing strong ONR and good agreement with solid curves in (E) and (G).

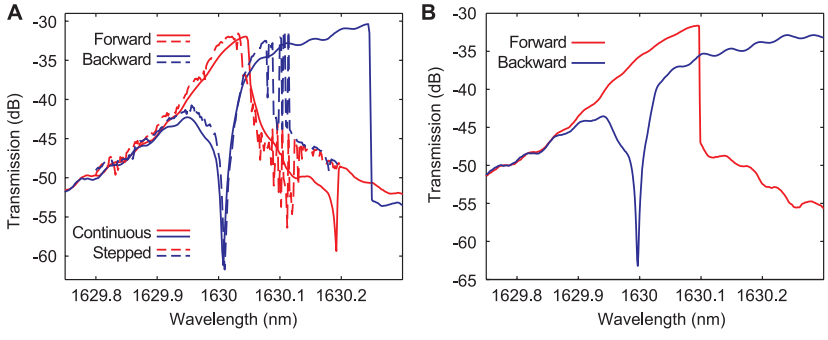

Fig. 2. Forward and backward transmission spectra of the all-silicon optical diode at relatively high input power levels. (**A**) Input power of ~850 μW (10 dBm at laser source). Solid curves denote data acquired through a continuous-mode scan; dashed lines denote data acquired through a stepped-mode scan. The NTR near 1630 nm is 27.3 dB for continuous-mode scan and 29 dB for stepped-mode scan. (**B**) Input power of ~2100 μW (14 dBm at laser source). The NTR near 1630 nm is 27 dB.

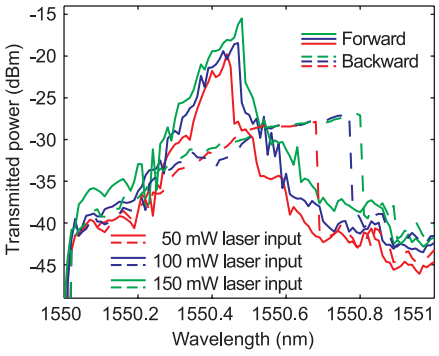

Fig. 3. Saturation of the backward-transmitted power near resonance in an ADF with coupling gaps of 420 nm and 630 nm.

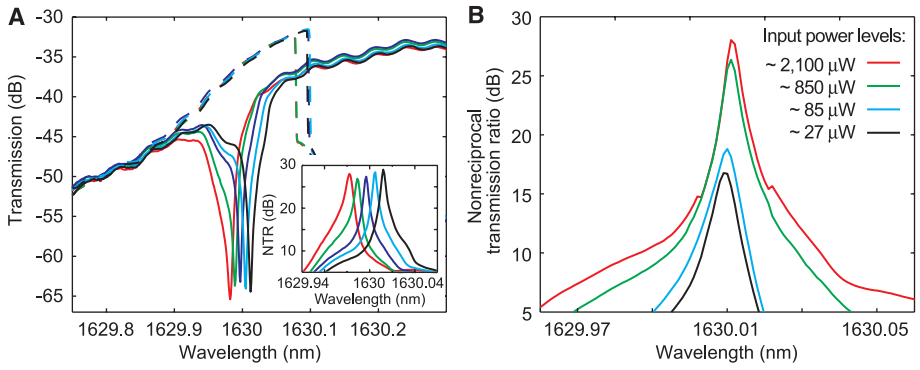

Fig. 4. (**A**) Wavelength tunability and tolerance of the mismatch between resonant wavelengths of the two filters. Dashed lines are forward transmissions; solid lines are backward transmissions. Input power was ~2100 μW. Inset explicitly shows the NTR. (**B**) The NTR at various input power levels with a fixed operating wavelength of 1630.011 nm.

sion in port II at λ_0 (solid curve in Fig. 1E). For backward propagation (input at port II), light will enter the ADF first. With the small gap, G_3, the energy in the ADF ring is high enough to red-shift its resonance—that is, $|\delta_{ADF,backward}(\lambda_0)| > 0$ in Eq. 4—and transmitted light at λ_0 will be reduced (Fig. 1F, solid curve). At the NF, the reduced light intensity, due to both the resonance shift and the insertion loss of the ADF, will not be able to red-shift the NF ring—that is, $\delta_{NF}(\lambda_0) \rightarrow 0$ in Eq. 5—and its intensity will be significantly reduced as it passes through the critically coupled NF at resonance ($\lambda_0 = \lambda_{NF}$, Fig. 1G).

At higher input power levels (~850 μW and ~2100 μW), larger NTRs up to 29 dB were observed (Fig. 2). This is due simultaneously to the increase of the NTR from the ADF (compared to Fig. 1F, which occurs at a rather moderate input power of ~85 μW) and to the sustained large NTR from the NF at high input power levels. Figure 3 shows the forward and backward transmissions of an individual ADF with coupling gaps of 420 nm and 630 nm (without a cascaded NF). In the forward direction, the transmitted power increases with the laser input power near resonance (~1550.4 nm), whereas the backward-transmitted power remains approximately the same, effectively increasing the NTR. In our optical diode (Fig. 1A), such saturation limits the backward input power entering the NF ($P_{c,b}$ in Fig. 1G). This restricts the nonlinearity in the NF and allows it to maintain high attenuation of the backward transmission.

The performance of our diode is independent of optical bistability (*7*, *20*, *26*) and is free from uncertainties caused by data acquisition schemes. In the spectra taken at two different scan modes of the tunable laser source (Fig. 2A), the solid lines are the spectra of a continuous-mode scan, which typically follows the upper trace of the hysteresis loop, whereas the dashed lines are the spectra of the stepped-mode scan (based on a step-by-step changing of operating wavelength), which generally follows the lower trace of the hysteresis loop. The rapid swing near 1630.1 nm indicates the transition between the upper and lower traces, possibly due to the fluctuations of laser power and wavelength in stepped-mode scan. Our optical diode does not operate in the bistability regime, and we observed almost identical NTRs with point measurements (i.e., fixing the laser at a specific wavelength and then measuring the transmitted power level at forward and backward directions) (table S1).

The device operation is robust against the mismatch of resonant wavelengths between the two filters, and it can achieve high NTR for various input power levels at a fixed wavelength. Within a resonance mismatch range of ~0.04 nm, the NTR remains over 25 dB (Fig. 4A). Given such tolerance, we were able to fix the operating wavelength of the diode by tuning the NF resonance in the backward direction to 1630.011 nm and achieved at least 18 dB of NTR for input power between 85 and 2100 μW (Fig. 4B).

An electronic diode blocks the backward current for a large range of applied backward voltages. Analogously, table S1 shows that our optical diode attenuates the backward-transmitted power to a low level (around –50 dBm) for a broad range of laser input power (5 to 14 dBm) at the operating wavelength of 1630.011 nm. The forward-transmitted power is more than 20 dB higher than the backward-transmitted power within this laser power range. Therefore, our optical diode tolerates not only input power variation, but also forward/backward input power disparity.

Similar to all resonance-enhanced optical devices, our all-silicon optical diode is bandwidth-limited. However, its operating wavelength can be thermally tuned (*19*) and should work across a large wavelength band. It also has a relatively high insertion loss after subtracting the coupling losses (~10.7 dB per facet). For laser input power levels between 5 and 10 dBm, the forward insertion losses were ~12 dB. This number could be reduced if the intrinsic quality factor of both rings is increased to 250,000 (*16*, *17*) and if the thermal isolation of the rings is improved, such as by suspending the NF ring away from the substrate (*27*).

The optical nonlinear effects in silicon include the Kerr effect (*28*, *29*), two-photon absorption (TPA) (*30*), the free carrier effect (FCE) (*31*), and the thermo-optic effect (*26*) from Joule heat generated through TPA, FCE, and linear absorption. Because of the large thermal dissipation time of the SiO_2 undercladding (~2 μs) (*21*–*23*) and the input power at tens of microwatts, the thermo-optic effect was dominant in our experiments. In addition to its role in enabling low-power operation, the thermo-optic effect (which reacts to optical powers averaged over a microsecond range) has a slow response time; this may benefit one-way transmission of data streams with high modulation speed, because the long integration time should desensitize nonlinear operation to fluctuations associated with rapidly varying data patterns or different modulation formats. Alternatively, when the slower thermal effect is mitigated through efficient thermal dissipation, fast nonlinearity such as FCE in silicon may dominate (*23*, *31*), opening doors to nonreciprocal high-speed optical signal processing where instantaneous response is required.

Our optical diode uses only the materials already used in CMOS processing and does not require external assistance such as magnetic fields, radio-frequency modulation, or optical pumping. The broad input power range within which our device performs may be sufficient for on-chip photonic applications. Its ability to block backward inputs that are much stronger than the forward inputs makes it functionally similar to electrical diodes. Our diode has an ultracompact footprint and is robust against resonance mismatch between the two microrings. These attributes make it attractive as a potential component for future highly integrated photonic information processing chips.

References and Notes

1. H. A. Haus, *Waves and Fields in Optoelectronics* (Prentice-Hall, Englewood Cliffs, NJ, 1984), pp. 56–61.
2. R. L. Espinola, T. Izuhara, M. C. Tsai, R. M. Osgood Jr., H. Dötsch, *Opt. Lett.* **29**, 941 (2004).
3. T. R. Zaman, X. Guo, R. J. Ram, *Appl. Phys. Lett.* **90**, 023514 (2007).
4. L. Bi *et al.*, *Nat. Photonics* **5**, 758 (2011).
5. S. F. Mingaleev, Y. S. Kivshar, *J. Opt. Soc. Am. B* **19**, 2241 (2002).

6. K. Gallo, G. Assanto, K. R. Parameswaran, M. M. Fejer, *Appl. Phys. Lett.* **79**, 314 (2001).
7. M. Soljačić, C. Luo, J. D. Joannopoulos, S. Fan, *Opt. Lett.* **28**, 637 (2003).
8. A. Rostami, *Opt. Laser Technol.* **39**, 1059 (2007).
9. S. K. Ibrahim, S. Bhandare, D. Sandel, H. Zhang, R. Noe, *Electron. Lett.* **40**, 1293 (2004).
10. J. Hwang *et al.*, *Nat. Mater.* **4**, 383 (2005).
11. S. Manipatruni, J. T. Robinson, M. Lipson, *Phys. Rev. Lett.* **102**, 213903 (2009).
12. Z. Yu, S. Fan, *Nat. Photonics* **3**, 91 (2009).
13. M. S. Kang, A. Butsch, P. S. J. Russell, *Nat. Photonics* **5**, 549 (2011).
14. B. E. Little, S. T. Chu, H. A. Haus, J. Foresi, J.-P. Laine, *J. Lightwave Technol.* **15**, 998 (1997).
15. Q. Xu, B. Schmidt, S. Pradhan, M. Lipson, *Nature* **435**, 325 (2005).
16. S. Xiao, M. H. Khan, H. Shen, M. Qi, *Opt. Express* **15**, 14467 (2007).
17. S. Xiao, H. Shen, M. H. Khan, M. Qi, *Conf. Lasers and Electro-Optics* CTuGG6 (2008); www.opticsinfobase.org/abstract.cfm?uri=CLEO-2008-CTuGG6.
18. T. Barwicz *et al.*, *Opt. Express* **12**, 1437 (2004).
19. M. H. Khan *et al.*, *Nat. Photonics* **4**, 117 (2010).
20. M. Soljačić, M. Ibanescu, S. G. Johnson, Y. Fink, J. D. Joannopoulos, *Phys. Rev. E* **66**, 055601 (2002).
21. P. E. Barclay, K. Srinivasan, O. Painter, *Opt. Express* **13**, 801 (2005).
22. T. Uesugi, B.-S. Song, T. Asano, S. Noda, *Opt. Express* **14**, 377 (2006).
23. Q. Xu, M. Lipson, *Opt. Lett.* **31**, 341 (2006).
24. J. Ouyang, X. Wang, M. Qi, Meep (MIT Electromagnetic Equation Propagation), http://nanohub.org/resources/2954 (2007).
25. See supporting material on *Science* Online.
26. V. R. Almeida, M. Lipson, *Opt. Lett.* **29**, 2387 (2004).
27. P. Sun, R. M. Reano, *Opt. Lett.* **35**, 1124 (2010).
28. X. Chen, N. C. Panoiu, I. Hsieh, J. I. Dadap, R. M. Osgood, *IEEE Photon. Technol. Lett.* **18**, 2617 (2006).
29. J. B. Driscoll *et al.*, *IEEE J. Sel. Top. Quantum Electron.* **16**, 1448 (2010).
30. M. Dinu, F. Quochi, H. Garcia, *Appl. Phys. Lett.* **82**, 2954 (2003).
31. A. C. Turner-Foster *et al.*, *Opt. Express* **18**, 3582 (2010).

Acknowledgments: We thank D. Leaird for experimental assistance and J. Ouyang for helpful discussions. Supported by Defense Threat Reduction Agency grant HDTRA1-10-1-0106, Air Force Office of Scientific Research grant FA9550-08-1-0379, NSF grant ECCS-0925759, and NIH grant 1R01RR026273-01. Finite-difference time domain simulation work was carried out through the Network for Computational Nanotechnology with resources available at www.nanohub.org. L.F. and L.T.V. fabricated and characterized the devices. J.W. performed simulation and selected device parameters. H.S. helped in device characterization. B.N. helped in the design. M.Q. conceived the idea and supervised the investigation. M.Q., L.T.V., L.F., and J.W. wrote the manuscript. All discussed the results and commented on the manuscript.

Supporting Online Material

www.sciencemag.org/cgi/content/full/science.1214383/DC1
Materials and Methods
Table S1

23 September 2011; accepted 6 December 2011
Published online 22 December 2011;
10.1126/science.1214383

Reversible Reduction of Oxygen to Peroxide Facilitated by Molecular Recognition

Nazario Lopez,[1] Daniel J. Graham,[1] Robert McGuire Jr.,[1] Glen E. Alliger,[1] Yang Shao-Horn,[2] Christopher C. Cummins,[1]* Daniel G. Nocera[1]*

Generation of soluble sources of peroxide dianion (O_2^{2-}) is a challenge in dioxygen chemistry. The oxidizing nature of this anion renders its stabilization in organic media difficult. This Report describes the chemically reversible reduction of oxygen (O_2) to cryptand-encapsulated O_2^{2-}. The dianion is stabilized by strong hydrogen bonds to N-H groups from the hexacarboxamide cryptand. Analogous stabilization of peroxide by hydrogen bonding has been invoked recently in crystalline saccharide and protein systems. The present peroxide adducts are stable at room temperature in dimethyl sulfoxide (DMSO) and *N*,*N*′-dimethylformamide (DMF). These adducts can be obtained in gram quantities from the cryptand-driven disproportionation reaction of potassium superoxide (KO_2) at room temperature.

Reduction of molecular oxygen to the level of peroxide dianion (O_2^{2-}) is typically accomplished in chemical and biological systems in the stabilizing coordination sphere of a transition metal (*1*). Such peroxide transition-metal complexes are important intermediates in natural oxidation processes (*2*–*4*), and they have long been used as reagents for organic synthesis (*5*). We hypothesized that peroxide dianion could be stabilized alternatively in a molecular environment of hydrogen bond donors so arranged as to completely surround O_2^{2-} with partial positive charge. A structural basis for peroxide stabilization via hydrogen bonding to organic matter has appeared recently in the context of sodium peroxide crystallization with 1,6-anhydro-β-maltose (*6*). The reported complex salt of formula $[Na_2(1,6\text{-anhydro-}\beta\text{-maltose})_2(H_2O)_3]O_2$ has a layered structure featuring six hydrogen bonds that encase each O_2^{2-} ion, with sugar O-H groups acting as the hydrogen-bond donors. This peroxide environment is reminiscent of that determined for $Na_2O_2 \cdot 8\,H_2O$, in which chains of edge-connected $[Na(OH_2)_6]^+$ octahedra are linked together by O–H···O peroxide/water hydrogen bonds (*7*). Now, we show that hexacarboxamide cryptand molecules of a type introduced originally as receptors for halide ions (*8*, *9*), and investigated by us as binucleating ligands for transition-metal ions (*10*, *11*), form soluble 1:1 complexes with peroxide dianion wherein O_2^{2-} resides in a molecular interior surrounded by six carboxamide N-H hydrogen bond donors in a trigonal antiprismatic array. The receptors stabilize peroxide dianion to such an extent that, if it is present in the same solution, superoxide (O_2^-) undergoes disproportionation to form O_2 and encapsulated O_2^{2-}, thus coupling the anion receptor molecular recognition phenomenon (*12*) to an oxidation-reduction process.

Preparation of the cryptand peroxide adduct can be achieved starting from either superoxide or O_2. Treatment of a slurry of *tert*-butyl–substituted hexacarboxamide cryptand (*m*BDCA-5t-H_6) with 2.2 equiv of KO_2 in *N*,*N*′-dimethylformamide (DMF) resulted in the formation of the O_2^{2-} adduct $[K_2(DMF)_5][(O_2)\subset m\text{BDCA-5t-}H_6]$ in 74% isolated yield (Fig. 1). Vigorous bubbling was observed immediately after adding KO_2; mass spectrometry (MS, fig. S1) establishes that the gas is a result of O_2 production from the cryptand-driven disproportionation of O_2^-. The ^{1}H nuclear magnetic resonance (NMR) spectrum (fig. S2) indicates the formation of a O_2^{2-} adduct in which the amide chemical shift is in the range of a normal charged hydrogen bond (NCHB) interaction (*13*). The generality of peroxide dianion recognition was probed by using the related 3,5-dipropoxyphenoxyl–substituted hexacarboxamide cryptand (*m*BDCA-5p-H_6) (*10*). Similar large downfield shifts of ^{1}H NMR signals for N-H [14.69 parts per million (ppm)] and aromatic protons (10.03 ppm) pointing inside the cavity were observed, indicative of O_2^{2-} encapsulation at room temperature (fig. S3). The $[(O_2)\subset m\text{BDCA-5t-}H_6]^{2-}$ adduct can also be obtained by reducing O_2 in situ with 2 equiv of cobaltocene ($CoCp_2$, where Cp is cyclopentadienyl) in the presence of 1 equiv of free cryptand in DMF (fig. S4), where the first reduction potential of $CoCp_2$ is coincident with the reduction of oxygen (fig. S5).

Both cryptand peroxide adducts were characterized by x-ray diffraction studies using single crystals obtained by vapor diffusion of diethyl ether into DMF solutions (Fig. 2 and figs. S6 and S7). A view down the pseudo-threefold axis of the adduct indicates that the cryptand adopts a propeller-like conformation (Fig. 2B and fig. S7b). The O–O bond lengths of 1.504 ± 0.0002 [1.504(2) (number in parentheses indicates the estimated standard deviation in the final digit) Å for $[K_2(DMF)_5][(O_2)\subset m\text{BDCA-5t-}H_6]$ and 1.499(2) Å for $(DMF)[K_2(DMF)_5][(O_2)\subset m\text{BDCA-5p-}H_6]$, which are comparable to that in ribonucleotide reductase Ib (1.47 Å) (*14*), in 1,6-anhydro-β-maltose adduct [1.496(2) Å] (*6*), and in Na_2O_2 (1.49 Å)

[1]Department of Chemistry, 77 Massachusetts Avenue, Massachusetts Institute of Technology (MIT), Cambridge, MA 02139–4307, USA. [2]Departments of Mechanical Engineering and Materials Science and Engineering, 77 Massachusetts Avenue, MIT, Cambridge, MA 02139–4307, USA.

*To whom correspondence should be addressed. E-mail: nocera@mit.edu (D.G.N.); ccummins@mit.edu (C.C.C.)